

## PAPER

View Article Online  
View Journal | View IssueCite this: *J. Mater. Chem. A*, 2022, 10, 24301

## Structural design strategies for superionic sodium halide solid electrolytes†

Seungho Yu,<sup>a</sup> Kwangnam Kim,<sup>c</sup> Brandon C. Wood,<sup>c</sup> Hun-Gi Jung<sup>ab</sup> and Kyung Yoon Chung<sup>ab</sup>

Sodium all-solid-state batteries (ASSBs) with superionic solid electrolytes (SEs) show substantial potential for large-scale energy-storage applications. Recently, lithium halide SEs have attracted attention owing to their potential compatibility with high-voltage cathode materials and high ionic conductivity. Although sodium halide SEs are believed to exhibit good electrochemical stability, very few compounds have been reported. This study provides design principles for superionic sodium halide SEs through systematic theoretical investigations of  $\text{Na}_3\text{MX}_6$  ( $\text{X} = \text{Cl}, \text{Br}, \text{and I}$ ). The  $\text{Na}_3\text{MX}_6$  structures depend on the types and sizes of  $\text{M}$  and  $\text{X}$ :  $\text{Na}_3\text{MCl}_6$  and  $\text{Na}_3\text{MBr}_6$  prefer the  $P\bar{3}1c$ ,  $P2_1/n$  and  $R\bar{3}$  phases, whereas  $\text{Na}_3\text{MI}_6$  prefers the  $C2/m$  phase. The  $\text{Na}_3\text{MI}_6$   $C2/m$  phase is found to exhibit reasonably high ionic conductivity ( $\sim 10^{-4} \text{ S cm}^{-1}$ ) and anion mixing with  $\text{Br}$  further improve  $\text{Na}$ -ion migration, leading to an even higher ionic conductivity ( $\sim 10^{-3} \text{ S cm}^{-1}$ ) for  $\text{Na}_3\text{MBr}_3\text{I}_3$ . The material design principles in this study provide fundamental guidelines for the development of superionic  $\text{Na}$  halide SEs for high-voltage  $\text{Na}$  ASSBs.

Received 28th June 2022

Accepted 3rd November 2022

DOI: 10.1039/d2ta05158c

rsc.li/materials-a

## Introduction

The development of next-generation batteries with high energy density and enhanced safety is required for emerging applications, such as energy storage systems (ESS) and electric vehicles.<sup>1</sup> All-solid-state batteries (ASSBs) with solid electrolytes (SEs) are promising candidates for next-generation batteries.<sup>2,3</sup> ASSBs resolve the safety concerns of conventional Li-ion batteries by replacing flammable liquid electrolytes with nonflammable inorganic SEs.<sup>4</sup> ASSBs with SEs also enable the use of metallic anodes that exhibit significantly higher energy densities than conventional anode materials.<sup>5</sup> Recently, various types of post-Li batteries with new cations such as  $\text{Na}$ ,  $\text{K}$ , and  $\text{Mg}$  have been investigated owing to their low cost and high energy density.<sup>6–11</sup> Among the post-Li batteries,  $\text{Na}$ -ion batteries have attracted increasing attention because of the abundance of  $\text{Na}$ .<sup>12,13</sup>  $\text{Na}$  ASSBs have been investigated for large-scale applications, such as ESS, which require high safety.<sup>14,15</sup>

Sulfide SEs have been widely studied for applications in  $\text{Na}$  ASSBs owing to their high ionic conductivity of  $1\text{--}10 \text{ mS cm}^{-1}$  for  $\text{Na}_3\text{PS}_4$ ,  $\text{Na}_3\text{SbS}_4$  and  $\text{Na}_{11}\text{Sn}_2\text{PS}_{12}$ .<sup>16–20</sup> However, sulfide SEs

are generally unstable in moisture and exhibit a narrow electrochemical stability window.<sup>21,22</sup> Oxide SEs (NASICONs and  $\beta$ -alumina) are chemically stable and can exhibit a high ionic conductivity of  $\sim 1 \text{ mS cm}^{-1}$ , but require a high-temperature sintering process to resolve the interfacial resistance.<sup>23,24</sup> Recently, halide SEs have been reported as promising SEs owing to their wide electrochemical stability window and compatibility with high-voltage cathode materials.<sup>25–28</sup> Li ternary chlorides,  $\text{Li}_3\text{MCl}_6$ , exhibit good chemical stability against high-voltage cathode materials ( $\sim 4 \text{ V}$ ) and have high ionic conductivity of  $0.5\text{--}3 \text{ mS cm}^{-1}$  for  $\text{Li}_3\text{YCl}_6$ ,  $\text{Li}_3\text{InCl}_6$  and  $\text{Li}_3\text{ScCl}_6$ .<sup>29–32</sup>

Although  $\text{Na}$  halides are expected to exhibit wide electrochemical stability,<sup>33</sup> very few  $\text{Na}$  halide SEs, such as  $\text{Na}_3\text{YCl}_6$ ,  $\text{Na}_3\text{ErCl}_6$ ,  $\text{Na}_2\text{ZrCl}_6$  and  $\text{Zr}$ -substituted  $\text{Na}_{3-x}\text{M}_{1-x}\text{Zr}_x\text{Cl}_6$  ( $\text{M} = \text{Y}$  and  $\text{Er}$ )—all of which have low ionic conductivity below  $10^{-4} \text{ S cm}^{-1}$ —have been reported.<sup>34–36</sup> Owing to the ionic radius of  $\text{Na}$  ( $102 \text{ pm}$ ), being larger than that of  $\text{Li}$  ( $76 \text{ pm}$ ),  $\text{Na}_3\text{MCl}_6$  exhibited different crystal structures of  $P\bar{3}1c$ ,  $P2_1/n$  and  $R\bar{3}$  with lower ionic conductivity than the crystal structures of  $\text{Li}_3\text{MCl}_6$ , such as  $C2/m$  and  $P\bar{3}m1$ .<sup>37</sup> Theoretical studies predicted the phase-dependent ionic conductivities of  $\text{Na}_3\text{YBr}_6$  and  $\text{Na}_3\text{YI}_6$ ,<sup>38,39</sup> but only a few studies have reported on the phases of  $\text{Na}$  bromides and iodides,  $\text{Na}_3\text{MX}_6$  ( $\text{X} = \text{Br}$  and  $\text{I}$ ).<sup>40</sup> This study aims to provide guidelines for the design of novel  $\text{Na}$  halide SEs,  $\text{Na}_3\text{MX}_6$  ( $\text{X} = \text{Cl}, \text{Br}$  and  $\text{I}$ ), through systematic investigations of their structural preference, phase stability, electrochemical stability and transport properties.

This study shows that the structures of  $\text{Na}_3\text{MX}_6$  are strongly dependent on the types and sizes of  $\text{M}$  and  $\text{X}$ . In particular,  $\text{Na}_3\text{MX}_6$  generally exhibited  $P\bar{3}1c$ ,  $P2_1/n$ ,  $R\bar{3}$  and  $C2/m$  phases,

<sup>a</sup>Energy Storage Research Center, Korea Institute of Science and Technology, 5, Hwarang-ro 14-gil, Seongbuk-gu, Seoul 02792, Republic of Korea. E-mail: shyu@kist.re.kr

<sup>b</sup>Division of Energy & Environment Technology, KIST School, Korea University of Science and Technology, Seoul 02792, Republic of Korea

<sup>c</sup>Materials Science Division, Lawrence Livermore National Laboratory, 94550, Livermore, USA

† Electronic supplementary information (ESI) available. See DOI: <https://doi.org/10.1039/d2ta05158c>

while  $\text{Na}_3\text{MX}_6$  with relatively small M cations preferred the  $\text{NaMX}_4$  ( $P2_12_12_1$ ) phase.<sup>41,42</sup>  $\text{Na}_3\text{MCl}_6$  and  $\text{Na}_3\text{MBr}_6$  preferred the  $P\bar{3}1c$ ,  $P2_1/n$  and  $R\bar{3}$  phases, with the phase transitions depending on the radius of M.  $\text{Na}_3\text{MI}_6$  preferred the  $C2/m$  phase and showed a high ionic conductivity ( $\sim 10^{-4} \text{ S cm}^{-1}$ ). Anion mixing with Br in  $\text{Na}_3\text{MI}_6$  further improved Na-ion migration, exhibiting a high ionic conductivity ( $\sim 10^{-3} \text{ S cm}^{-1}$ ) that is two orders of magnitude higher than the value reported for competing Na halide SEs. The material design principles in this study offer substantial promise for the development of practical superionic Na halide SEs.

## Methods

First principles calculations were performed based on the density functional theory (DFT) with a plane-wave basis set, as implemented in the Vienna *Ab initio* Simulation Package (VASP).<sup>43,44</sup> The projector augmented wave method (PAW) was used for the core and valence electron interactions<sup>45</sup> and the generalized gradient approximation (GGA) of Perdew–Burke–Ernzerhof (PBE) was employed for the exchange–correlation energy functional.<sup>46</sup> A van der Waals (vdW) density functional (optB86b-vdW) was used to address vdW interactions in layered Na halide structures.<sup>47</sup> An energy cutoff of 520 eV was used for the plane-wave basis sets and the  $k$ -point mesh was determined using the Python Materials Genomics (pymatgen) package,<sup>48</sup> including a  $k$ -point density of at least 1000 per atom. Ionic relaxations were performed until the forces were less than  $0.01 \text{ eV \AA}^{-1}$ , with a convergence criterion of  $10^{-5} \text{ eV}$  for the electronic self-consistency loop.

The simulation cells of sodium halides  $\text{Na}_3\text{MX}_6$  ( $X = \text{Cl, Br and I}$ ) were generated based on the experimental structures of  $\text{Na}_3\text{MX}_6$  that exhibited trigonal  $P\bar{3}1c$  (#163),<sup>49,50</sup> monoclinic  $P2_1/n$  (#14),<sup>34,35</sup> trigonal  $R\bar{3}$  (#148)<sup>51</sup> and monoclinic  $C2/m$  (#12)<sup>29</sup> crystal structures. The trigonal  $P\bar{3}m1$  (#164) Li chloride structure,  $\text{Li}_3\text{MX}_6$ ,<sup>27</sup> was also used to prepare  $\text{Na}_3\text{MX}_6$  simulation cells. Among the possible ionic configurations for the partially occupied sites in the  $R\bar{3}$ ,  $P2_1/n$  and  $P\bar{3}m1$  phases, the  $\text{Na}_3\text{MX}_6$  structure with the lowest total energy was used for subsequent calculations. Details of the structural information of  $C2/m$  and  $P\bar{3}m1$  phases are provided in Table S1.† Various metal elements in +3 oxidation states have been considered for ternary metal halides,  $\text{Na}_3\text{MX}_6$ , including group 3 elements (Sc, Lu and Y), group 13 elements (Al, Ga, In and Tl), group 15 elements (Bi) and lanthanides (Yb, Tm, Er, Ho, Dy, Tb, Gd, Sm, Nd and La). The transition metals with multiple oxidation states were excluded in this study. The phase stability of  $\text{Na}_3\text{MX}_6$  ( $X = \text{Cl, Br and I}$ ) was evaluated by calculating the decomposition energy,  $E_d$ , against the competing stable phases  $\text{NaX}$  and  $\text{MX}_3$ . The metastable  $\text{Na}_3\text{MX}_6$  phase with an  $E_d$  below 25 meV per atom was considered to be a stable phase, owing to stabilization by entropic effects and kinetic inhibition. Further experimental studies can be performed to identify the stable structure of  $\text{Na}_3\text{MX}_6$ , based on the theoretical works.

The Na-ion potential energy landscape in  $\text{Na}_3\text{MX}_6$  was obtained using the bond-valence site energy (BVSE) method, as implemented in SoftBV software.<sup>52</sup> The potential energy of the

Na sites was calculated using the Morse-type interaction potential with a grid density of  $0.1 \text{ \AA}$ . The Na-ion migration path was predicted using the isosurface of the Na-ion probability density and the minimum energy value between the migration paths for the Na-ion migration energy barrier was obtained. Na-ion diffusivity in  $\text{Na}_3\text{MX}_6$  was examined using *ab initio* molecular dynamics (AIMD) simulations with an energy cutoff of 350 eV,  $\Gamma$ -point-only  $k$ -point grid and the NVT ensemble with a Nosé–Hoover thermostat. A  $2 \times 2 \times 1$  supercell was used for  $P\bar{3}1c$ ,  $P2_1/n$  and  $R\bar{3}$ , and a  $2 \times 1 \times 2$  supercell was used for the  $C2/m$  structure for the AIMD calculations corresponding to 80 atoms for the  $P\bar{3}1c$ ,  $P2_1/n$  and  $C2/m$ , and 120 atoms for  $R\bar{3}$  structures. The Na-ion diffusivity was evaluated using the mean squared displacement (MSD) at five different temperatures (700, 750, 800, 900 and 1000 K) for a window of 100 to 200 ps, with a time step of 2 fs. Data from the AIMD simulations were analyzed using the diffusion analysis module of the pymatgen package.<sup>48</sup> The total mean squared displacement (TMSD) and effective ion jumps were calculated to evaluate the relative standard deviation of diffusivity based on previous studies.<sup>53,54</sup> The diffusion coefficient,  $D$ , was derived using the TMSD of Na ions as a function of the time interval,  $\Delta t$ :

$$D = \frac{1}{2d\Delta t} \frac{\text{TMSD}(\Delta t)}{n} = \frac{1}{2d\Delta t n} \sum_{i=1}^n \frac{1}{N_{\Delta t}} \sum_{t=0}^{t_{\text{tot}}-\Delta t} |r_i(t + \Delta t) - r_i(t)|^2 \quad (1)$$

where  $d$  is the dimensionality,  $n$  is the total number of Na ions,  $N_{\Delta t}$  is the total number of time intervals and  $r_i$  is the Na ion trajectory. The ionic conductivity,  $\sigma$ , was calculated using the Nernst–Einstein equation:

$$\sigma = \frac{(ze)^2 c D}{k_B T} \quad (2)$$

where  $z$  is the valence of the ion,  $e$  is the elementary charge,  $c$  is the concentration of the ion,  $D$  is the diffusion coefficient,  $k_B$  is the Boltzmann constant and  $T$  is the temperature. Na-ion migration trajectories during the AIMD simulations were observed using a  $25 \times 25 \times 25$  grid mesh. Isosurfaces of the ionic probability densities were obtained to visualize ion migration using the mean ionic probability density ( $P_0$ ).

The electrochemical stability of  $\text{Na}_3\text{MX}_6$  ( $X = \text{Cl, Br and I}$ ) was investigated using the Materials Project (MP) database.<sup>55</sup> The grand potential phase diagram as a function of the chemical potential of Na was obtained using the pymatgen package<sup>48</sup> to evaluate the electrochemical stability window of  $\text{Na}_3\text{MX}_6$ . The total energies of  $\text{Na}_3\text{MX}_6$  were updated using equivalent settings in the MP for the calculations. The oxidation and reduction potentials with their phase equilibria were examined to determine the electrochemical stability of  $\text{Na}_3\text{MX}_6$ .  $\text{Na}_3\text{MX}_6$  compounds that were unstable against phase decomposition were excluded from the electrochemical stability calculations.

## Results

The most stable structure of  $\text{Na}_3\text{MX}_6$  ( $X = \text{Cl, Br and I}$ ) among trigonal  $P\bar{3}1c$ , monoclinic  $P2_1/n$ , trigonal  $R\bar{3}$ , monoclinic  $C2/m$

and trigonal  $\bar{P}3m1$  was determined by comparing the total energies of the phases, as shown in Fig. S1–S3 and Table S2.† Although the energy differences among the phases are small and several phases can be considered as the most stable phase, there exists a general trend for phase transitions among the structures, as a function of the size of cation (M) and anion (X). The phase preference for  $\text{Na}_3\text{MCl}_6$  agrees with a previous work<sup>37</sup> showing that  $\text{Na}_3\text{MCl}_6$  with relatively small M cations prefers the trigonal  $\bar{P}31c$  phase, whereas  $\text{Na}_3\text{MCl}_6$  with modestly large M cations prefers the monoclinic  $P2_1/n$  phase and  $\text{Na}_3\text{MCl}_6$  with even larger M cations above 90 pm prefers the  $R\bar{3}$  phase, as shown in Fig. S1.† The phase preference of  $\text{Na}_3\text{MBr}_6$  was found to be comparable to that of  $\text{Na}_3\text{MCl}_6$  in the  $\bar{P}31c$ ,  $P2_1/n$  and  $R\bar{3}$  phases; however, the driving force for the phase transitions to  $P2_1/n$  and  $R\bar{3}$  for  $\text{Na}_3\text{MBr}_6$  was relatively weaker than for  $\text{Na}_3\text{MCl}_6$ , as shown in Fig. S1.† Therefore, phase transitions (from  $\bar{P}31c$  to  $P2_1/n$  and from  $P2_1/n$  to  $R\bar{3}$ ) require relatively larger M cations in  $\text{Na}_3\text{MBr}_6$  compared with  $\text{Na}_3\text{MCl}_6$ .  $\text{Na}_3\text{MCl}_6$  and  $\text{Na}_3\text{MBr}_6$  preferred  $\bar{P}31c$ ,  $P2_1/n$  and  $R\bar{3}$  phases, while  $\text{Na}_3\text{MI}_6$  preferentially exhibited the  $C2/m$  phase over the other phases. The energy difference plot in Fig. S2† shows this phase preference of  $C2/m$  compared with other phases for  $\text{Na}_3\text{MI}_6$ . The energy differences for the  $\bar{P}31c$ ,  $P2_1/n$ ,  $R\bar{3}$ ,  $C2/m$  and  $\bar{P}3m1$  phases for  $\text{Na}_3\text{MX}_6$  (X = Cl, Br and I) are listed in Table S2.† The energy difference among the phases was negligible for  $\text{Na}_3\text{MBr}_6$  since they were in the phase transition region. The ground state of structure with the lowest energy should be examined to obtain the accurate results.

The phase stability of  $\text{Na}_3\text{MX}_6$  (X = Cl, Br and I) was evaluated using the decomposition energy,  $E_d$ , against the competing stable phases,  $\text{NaX}$  and  $\text{MX}_3$ . The most stable phase of  $\text{MX}_3$  among the experimental structures listed in Tables S3 and S4† was used to evaluate  $E_d$ . The  $E_d$  values for the  $\bar{P}31c$ ,  $P2_1/n$ ,  $R\bar{3}$ ,  $C2/m$  and  $\bar{P}3m1$  structures are illustrated as a heat map in Fig. S3 and S4.†  $\text{Na}_3\text{MX}_6$  phases with negative  $E_d$  values (dark blue) were considered stable against decomposition to  $\text{NaX}$  and  $\text{MX}_3$ , whereas  $\text{Na}_3\text{MX}_6$  phases with positive  $E_d$  values under 25 meV per atom were considered metastable phases owing to the entropic effects and kinetic barrier of decomposition.  $\text{Na}_3\text{MX}_6$  phases with positive  $E_d$  values above 25 meV per atom (light brown) were considered unstable phases, which generally included large M cations ( $M_{\text{radii}} > 95$  pm), such as Sm, Nd and La.  $\text{Na}_3\text{MCl}_6$  typically exhibit stable phases, whereas most  $\text{Na}_3\text{MBr}_6$  and  $\text{Na}_3\text{MI}_6$  exhibit metastable or unstable phases. The  $\text{Na}_3\text{MI}_6$   $E_d$  values are higher than those for  $\text{Na}_3\text{MBr}_6$ , suggesting that the relatively large X in  $\text{Na}_3\text{MX}_6$  decreases phase stability. The most stable  $\text{Na}_3\text{MX}_6$  phases with the lowest  $E_d$  value among the  $\bar{P}31c$ ,  $P2_1/n$ ,  $R\bar{3}$ ,  $C2/m$  and  $\bar{P}3m1$  phases are shown in Fig. 1(a) and Tables S5 and S6.†

The  $\text{Na}_3\text{MX}_6$  structures are strongly dependent on the sizes of M and X. The octahedral factor,  $t$ , was employed to investigate the structural preferences of  $\text{Na}_3\text{MX}_6$ . Defined as the ratio of the radius of cation to anion ( $r^+/r^-$ ), this octahedral factor between M and X ( $t_{\text{MX}} = r_{\text{M}}/r_{\text{X}}$ ) effectively described the structure of the Li–M–X compound in an earlier study.<sup>25,56</sup> Li–M–X was found to form  $\text{MX}_8$  cubes for high values of  $t_{\text{MX}}$ , such as fluorides, while the structures changed to  $\text{MX}_6$  octahedra for

lower values of  $t_{\text{MX}}$ , such as chlorides ( $\text{Li}_3\text{MCl}_6$ ). The Li–M–X compound exhibited an  $\text{MX}_4$  tetrahedron upon further decrease in  $t_{\text{MX}}$ , forming  $\text{LiMX}_4$ .<sup>25,56</sup> The M–X structural changes in the Na–M–X compounds were consistent with these prior results for the Li–M–X compounds, suggesting that moderate values of  $t_{\text{MX}}$  result in  $\text{Na}_3\text{MX}_6$  phases, whereas lower values of  $t_{\text{MX}}$  result in  $\text{NaMX}_4$  phases. Na–M–X compounds with relatively small cations, such as Al and Ga, showed low  $t_{\text{MX}}$  values, exhibiting the  $\text{NaMX}_4$  ( $P2_12_12_1$ ) phase instead of the  $\text{Na}_3\text{MX}_6$  phase, as shown in Table S7.†

The octahedral factor between A and X ( $t_{\text{AX}} = r_{\text{A}}/r_{\text{X}}$ , A = Li and Na) and  $t_{\text{MX}}$  was evaluated to investigate the structure of  $\text{Na}_3\text{MX}_6$  in Fig. 1(b–d). Using the  $t_{\text{AX}}$  and  $t_{\text{MX}}$  as  $x$  and  $y$  values in the two-dimensional plot in Fig. 1(b), the structural preferences of  $\text{A}_3\text{MX}_6$  among the  $\bar{P}31c$ ,  $P2_1/n$ ,  $R\bar{3}$ ,  $C2/m$  and  $\bar{P}3m1$  phases were assessed. Data that lie on the dashed line in Fig. 1(b) feature  $t_{\text{AX}}$  that is equivalent to  $t_{\text{MX}}$ , indicating that the sizes of octahedra of  $\text{MX}_6$  and  $\text{AX}_6$  are comparable (e.g.,  $\text{Li}_3\text{ScCl}_6$ ). Data points for  $\text{A}_3\text{MX}_6$  lie above or below this dashed line when the size of M is larger or smaller than A, respectively.  $\text{Na}_3\text{MX}_6$  (X = Cl, Br and I) is positioned below the dashed line because the ionic radius of Na (102 pm) is typically larger than that of the M cations. Most Li chlorides and bromides,  $\text{Li}_3\text{MX}_6$  (X = Cl and Br), were found to lie above the dashed line because of the smaller ionic radius of Li (76 pm) compared with that of the M cations. Li fluorides and iodides ( $\text{Li}_3\text{MX}_6$ , X = F and I) were disregarded in this plot because they exceeded the span of  $t$  for  $\text{Na}_3\text{MX}_6$ , exhibiting high values of  $t_{\text{MX}}$  above 0.6 for  $\text{Li}_3\text{MF}_6$  and low values of  $t_{\text{AX}}$  under 0.35 for  $\text{Li}_3\text{MI}_6$ .

In Fig. 1(b), the  $\text{NaMX}_4$  ( $P2_12_12_1$ ) phase for relatively small M cations with low values of  $t_{\text{MX}}$  in Table S7† is represented in yellow. For  $\text{Na}_3\text{MX}_6$  with higher values of  $t_{\text{MX}}$  than those of  $\text{NaMX}_4$ , the most stable structural phase among  $\bar{P}31c$ ,  $P2_1/n$ ,  $R\bar{3}$ ,  $C2/m$  and  $\bar{P}3m1$  is represented by black, red, blue, green and purple, respectively.  $\text{Li}_3\text{MX}_6$  compounds (X = Cl and Br) generally exhibited the  $C2/m$  phase, whereas the  $\bar{P}3m1$  phase was the stable phase for  $\text{Li}_3\text{MCl}_6$  with large M cations, corresponding to a high  $t_{\text{MX}}$  above 0.5.<sup>57</sup>  $\text{Na}_3\text{MI}_6$  showed similar values of  $t_{\text{AX}}$  and  $t_{\text{MX}}$  ( $t_{\text{AX}} \sim 0.45$  and  $0.35 < t_{\text{MX}} < 0.5$ ) to  $\text{Li}_3\text{MCl}_6$ , resulting in a preference for the  $C2/m$  phase. As the size of the X anion increases ( $t_{\text{AX}} > 0.5$ ),  $\text{Na}_3\text{MX}_6$  (X = Cl and Br) was found to prefer the  $\bar{P}31c$ ,  $P2_1/n$  and  $R\bar{3}$  phases to the  $C2/m$  phase, with  $\bar{P}31c$ – $P2_1/n$ – $R\bar{3}$  phase transitions occurring for  $\text{Na}_3\text{MX}_6$  (X = Cl and Br) with increased size of M (i.e., with larger  $t_{\text{MX}}$ ).

The phase preferences of  $\text{A}_3\text{MX}_6$  (A = Li and Na; X = Cl, Br and I) with M in the p-block (groups 13 and 15; M = Al, Ga, In, Tl and Bi) was observed to be slightly different, with phase transitions (from  $P2_12_12_1$  to  $C2/m$ , from  $P2_12_12_1$  to  $\bar{P}31c$ , from  $\bar{P}31c$  to  $P2_1/n$ ) occurring with relatively large M cations. For example, the group 3 element Sc (75 pm) exhibited phase transitions from  $P2_12_12_1$  to  $\bar{P}31c$  for  $\text{Na}_3\text{ScCl}_6$  and from  $\bar{P}31c$  to  $P2_1/n$  for  $\text{Na}_3\text{ScCl}_6$ , whereas the group 13 element In, with a relatively large ionic radius (80 pm), exhibited  $P2_12_12_1$  for  $\text{NaInI}_4$  and  $\bar{P}31c$  for  $\text{Na}_3\text{InCl}_6$ . The difference in electronegativity between M and X is smaller for the p-block elements than for the d- and f-block elements (i.e., group 3 elements and lanthanides), resulting in weaker Coulomb interactions and different phase-transition



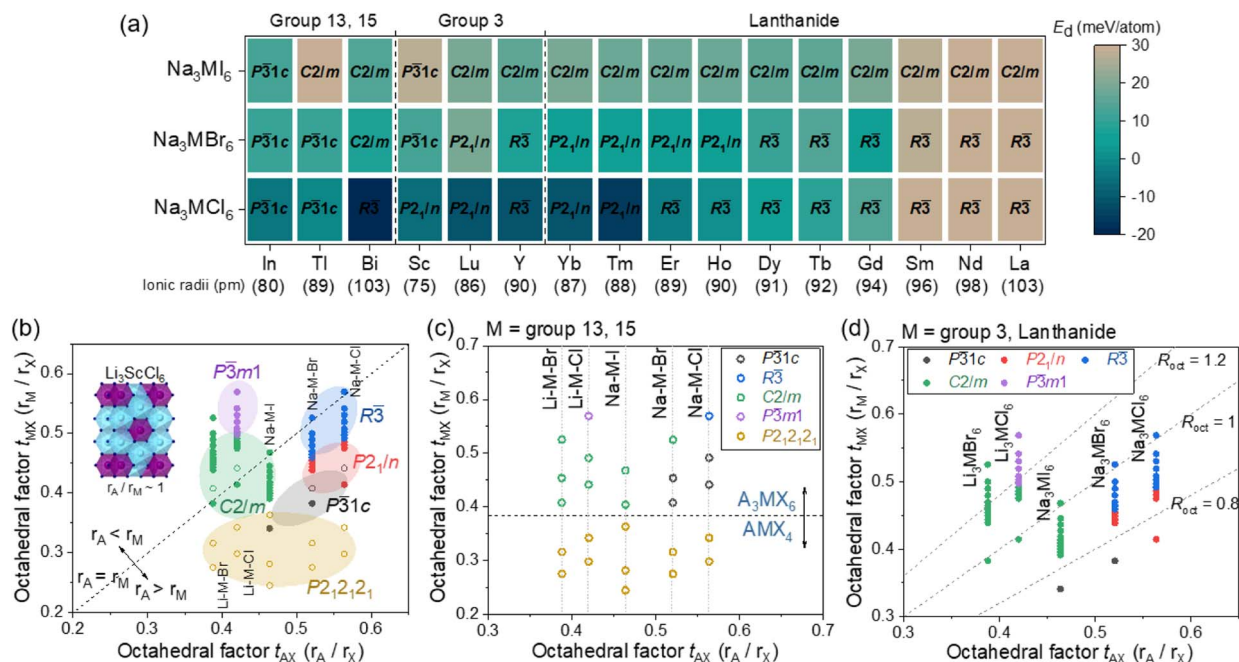


**Fig. 1** (a) Heat map for the decomposition energy ( $E_d$ ) of Na halides ( $\text{Na}_3\text{MX}_6$ , X = Cl, Br and I) against the competing phases NaX and  $\text{MX}_3$ . The most stable phase for the crystal structures of  $\text{P}\bar{3}1\text{c}$ ,  $\text{P}2_1/\text{n}$ ,  $\text{R}\bar{3}$ ,  $\text{C}2/\text{m}$  and  $\text{P}3\text{m}1$  was used to evaluate  $E_d$  for  $\text{Na}_3\text{MX}_6$ . (b–d) Structural preference tendencies of the crystal systems for  $\text{P}\bar{3}1\text{c}$ ,  $\text{P}2_1/\text{n}$ ,  $\text{R}\bar{3}$ ,  $\text{C}2/\text{m}$ ,  $\text{P}3\text{m}1$  and  $\text{P}2_12_12_1$  as a function of the octahedral factors for  $\text{AX}_6$  ( $r_{\text{A}}/r_{\text{X}}$ ) and  $\text{MX}_6$  ( $r_{\text{M}}/r_{\text{X}}$ ) for Li and Na metal ternary halides based on M elements: (b) all elements, (c) group 13 and 15 elements, (d) group 3 and lanthanide elements. Compounds in same composition group (A–M–X) are aligned vertically in (b–d).  $R_{\text{oct}}$  in (d) corresponds to the ratio of  $r_{\text{A}}$  to  $r_{\text{M}}$ .

trends.<sup>57</sup> Hence, the phase transitions of  $\text{A}_3\text{MX}_6$  with p-block elements occurred only with a relatively large M, for which the difference in electronegativity becomes appreciable. The data for  $\text{A}_3\text{MX}_6$  with p-block elements are presented using open symbols in Fig. 1(b and c) and the phase preferences of  $\text{A}_3\text{MX}_6$  in Fig. 1(b) are divided into two plots based on the M cation: Fig. 1(c) for group 13 and 15 elements and Fig. 1(d) for group 3 and lanthanide elements.

Fig. 1(c) shows the preference of the  $\text{MX}_4$  tetrahedron for relatively small p-block elements with low values of  $t_{\text{MX}}$  ( $<0.38$ ), forming the  $\text{NaMX}_4$  ( $\text{P}2_12_12_1$ ) phase. Because this  $\text{P}2_12_12_1$  phase includes  $\text{MX}_4$  tetrahedron showing low ionic conductivity,<sup>26</sup> M cations with small ionic radii may be neglected in the design of superionic Na–M–X SEs. The phase preference of  $\text{A}_3\text{MX}_6$  for group 3 elements and lanthanides with relatively large ionic radii ( $>74$  pm) is shown in Fig. 1(d). Here, the ratio of octahedral factors,  $R_{\text{oct}} = t_{\text{MX}}/t_{\text{AX}} = r_{\text{M}}/r_{\text{A}}$  was used to classify the  $\text{A}_3\text{MX}_6$  phases. The value of  $R_{\text{oct}}$  is higher or lower than 1 when the cation M is larger or smaller than A, respectively. The  $R_{\text{oct}}$  values were generally 1.0–1.3 for  $\text{Li}_3\text{MCl}_6$  and they exhibited a phase transition from  $\text{C}2/\text{m}$  to  $\text{P}3\text{m}1$  at a  $R_{\text{oct}}$  value of approximately 1.2. The  $R_{\text{oct}}$  values were generally 0.8–1.0 for  $\text{Na}_3\text{MX}_6$  (X = Cl, Br and I) because of the large ionic radius of Na (102 pm).  $\text{Na}_3\text{MI}_6$  maintained the  $\text{C}2/\text{m}$  phase in this range, whereas  $\text{Na}_3\text{MBr}_6$  and  $\text{Na}_3\text{MCl}_6$  exhibited a phase transition from  $\text{P}2_1/\text{n}$  to  $\text{R}\bar{3}$  phase at  $R_{\text{oct}}$  values of approximately 0.85.

The Na-ion potential energy landscapes for the  $\text{P}\bar{3}1\text{c}$ ,  $\text{P}2_1/\text{n}$  and  $\text{R}\bar{3}$  phases of  $\text{Na}_3\text{MX}_6$  (Cl and Br) and the  $\text{C}2/\text{m}$  phase of  $\text{Na}_3\text{MI}_6$  were predicted using the BVSE method. The

experimental structures of  $\text{Na}_3\text{InCl}_6$ ,  $\text{Na}_3\text{ErCl}_6$ ,  $\text{Na}_3\text{GdCl}_6$  and  $\text{Na}_3\text{GdI}_6$  were used to examine Na-ion migration in the  $\text{P}\bar{3}1\text{c}$ ,  $\text{P}2_1/\text{n}$ ,  $\text{R}\bar{3}$  and  $\text{C}2/\text{m}$  phases, respectively. The isosurface of the Na-site energy (light blue) was obtained to visualize the Na-ion migration pathways, as shown in Fig. 2 and S5–S9.† The calculation results indicate that the trigonal  $\text{P}\bar{3}1\text{c}$  and  $\text{R}\bar{3}$  phases of  $\text{Na}_3\text{MCl}_6$  show 1D paths between octahedral sites (Oct.–Oct.) along the z-axis as well as 3D paths between octahedral sites *via* tetrahedral interstitial sites (Oct.–Tet.–Oct.). The monoclinic  $\text{P}2_1/\text{n}$  phase of  $\text{Na}_3\text{MCl}_6$  exhibits 3D paths between octahedral and prism sites (Oct.–Prism) and between octahedral and prism sites *via* tetrahedral interstitial sites (Oct.–Tet.–Prism), agreeing with previous studies.<sup>37</sup> The Na-ion migration paths in  $\text{Na}_3\text{InBr}_6$  ( $\text{P}\bar{3}1\text{c}$ ),  $\text{Na}_3\text{ErBr}_6$  ( $\text{P}2_1/\text{n}$ ) and  $\text{Na}_3\text{GdBr}_6$  ( $\text{R}\bar{3}$ ) were found to be consistent with the paths in  $\text{Na}_3\text{MCl}_6$ , as shown in Fig. 2, while the energy barrier between the migration paths was slightly decreased compared to  $\text{Na}_3\text{MCl}_6$  (Fig. S5†). The Na-ion migration paths in  $\text{Na}_3\text{GdI}_6$  for the  $\text{C}2/\text{m}$  phase include three-dimensional paths between octahedral sites connected by tetrahedral interstitial sites (Oct.–Tet.–Oct.). Details of the migration paths in  $\text{Na}_3\text{InBr}_6$  ( $\text{P}\bar{3}1\text{c}$ ),  $\text{Na}_3\text{ErBr}_6$  ( $\text{P}2_1/\text{n}$ ),  $\text{Na}_3\text{GdBr}_6$  ( $\text{R}\bar{3}$ ) and  $\text{Na}_3\text{GdI}_6$  ( $\text{C}2/\text{m}$ ) are presented in Fig. S6–S9,† respectively.

The Na-ion migration energy barriers ( $E_a$ ) in the  $\text{P}\bar{3}1\text{c}$ ,  $\text{P}2_1/\text{n}$  and  $\text{R}\bar{3}$  phases of  $\text{Na}_3\text{MX}_6$  (M = In, Er, Gd; X = Cl, Br) and the  $\text{C}2/\text{m}$  phase of  $\text{Na}_3\text{GdI}_6$  were predicted using BVSE, as shown in Fig. 2 and S5.† The trigonal  $\text{P}\bar{3}1\text{c}$  and  $\text{R}\bar{3}$  phases of  $\text{Na}_3\text{MCl}_6$  exhibited  $E_a$  of 0.45 and 0.35 eV, respectively, for the 1D paths between face sharing octahedral sites (Na1–i1), and  $E_a$  of 0.53



Fig. 2 Na-ion potential energy landscape of (a)  $\text{Na}_3\text{InBr}_6$  (trigonal  $\bar{P}31c$ ), (b)  $\text{Na}_3\text{ErBr}_6$  (monoclinic  $P2_1/n$ ), (c)  $\text{Na}_3\text{GdBr}_6$  (trigonal  $R\bar{3}$ ) and (d)  $\text{Na}_3\text{GdI}_6$  (monoclinic  $C2/m$ ) calculated using the BVSE method, including Na-ion migration energy barriers along the migration paths. Details of migration paths are shown in Fig. S6–S9.†

and 0.65 eV, respectively, for the 3D paths between octahedral sites through the interstitial tetrahedral site (i1–i2–Na2 and Na1–i2–Na2). Note that  $E_a$  for the 3D paths is the key determiner for long-range migration rates. The  $E_a$  values in the  $P2_1/n$  phase of  $\text{Na}_3\text{MCl}_6$  were 0.60 eV for migration paths between octahedral and prism sites through tetrahedral interstitial sites (Na1–i1–i2–Na2) and 0.70 eV for the migration paths between octahedral and prism sites (Na2–Na3). The higher values of  $E_a$  for the  $R\bar{3}$  and  $P2_1/n$  phases indicate that the Na-ion diffusivity would be reduced for those phases. The  $\bar{P}31c$ ,  $P2_1/n$  and  $R\bar{3}$  phases of  $\text{Na}_3\text{MBr}_6$  exhibited slightly lower  $E_a$  than those of  $\text{Na}_3\text{MCl}_6$  as shown in Fig. 2. The  $E_a$  for the 3D paths in the  $\bar{P}31c$ ,  $P2_1/n$  and  $R\bar{3}$  phases of  $\text{Na}_3\text{MBr}_6$  were 0.49, 0.54 and 0.52 eV, respectively, suggesting an improvement in Na-ion migration in  $\text{Na}_3\text{MBr}_6$ . The  $E_a$  value for the  $C2/m$  phase of  $\text{Na}_3\text{GdI}_6$  was computed as 0.48 eV for the 3D paths between octahedral sites through the interstitial tetrahedral sites (Na1–i1–i2), indicating that Na-ion diffusivity in the  $C2/m$  phase would be higher than in other phases. The  $E_a$  value for the 1D and 3D paths of  $\text{Na}_3\text{MX}_6$  ( $\text{M} = \text{In, Er, Gd}$ ;  $\text{X} = \text{Cl, Br}$ ) and  $\text{Na}_3\text{GdI}_6$  are listed in Table S8.†

In addition to simple empirical BVSE calculations,<sup>58,59</sup> further detailed analysis of Na-ion migration in the  $\bar{P}31c$ ,  $P2_1/n$  and  $R\bar{3}$  phases of  $\text{Na}_3\text{MX}_6$  ( $\text{X} = \text{Br}$  and  $\text{I}$ ) were performed using AIMD simulations. The Na-ion diffusivity in  $\text{Na}_3\text{InBr}_6$  ( $\bar{P}31c$ ),  $\text{Na}_3\text{ErBr}_6$  ( $P2_1/n$ ),  $\text{Na}_3\text{GdBr}_6$  ( $R\bar{3}$ ),  $\text{Na}_3\text{YI}_6$  ( $C2/m$ ) and  $\text{Na}_3\text{GdI}_6$  ( $C2/m$ ) were evaluated using the Na-ion mean squared displacement (MSD), as shown in Fig. S10.†  $\text{Na}_3\text{ErBr}_6$  ( $P2_1/n$ ) showed negligible Na-ion MSD over 100 ps at 900 K (Fig. S11†), suggesting the low ionic conductivity of  $\text{Na}_3\text{MBr}_6$  with  $P2_1/n$  structure. According to earlier studies, the ionic conductivity of  $\text{Na}_3\text{ErBr}_6$  should be approximately  $10^{-9} \text{ S cm}^{-1}$ , reflecting the fact that inter-site hopping was not observed in the MSD plot at 900 K.<sup>60</sup> The Na-ion diffusivities of  $\text{Na}_3\text{MBr}_6$  were improved in

the  $\bar{P}31c$  and  $R\bar{3}$  phases, and  $\bar{P}31c$  showed the highest diffusivity among the  $\bar{P}31c$ ,  $P2_1/n$  and  $R\bar{3}$  phases of  $\text{Na}_3\text{MBr}_6$ . Note that, in Fig. 3(a), the Na-ion diffusivities of  $\text{Na}_3\text{InBr}_6$  ( $\bar{P}31c$ ) at 900 and 1000 K (open triangles) are extrapolated values from the lower-temperature simulations because  $\text{Na}_3\text{InBr}_6$  melted at high temperature.

As shown in Fig. 3(b),  $\text{Na}_3\text{GdBr}_6$  ( $R\bar{3}$ ) exhibited activation energy of 0.50 eV and ionic conductivity of  $1.2 \times 10^{-6} \text{ S cm}^{-1}$  at room temperature. Na-ion MSD was found to further improve in  $\text{Na}_3\text{InBr}_6$  ( $\bar{P}31c$ ), exhibiting activation energy of 0.37 eV and ionic conductivity of  $5.8 \times 10^{-5} \text{ S cm}^{-1}$  at room temperature. The  $C2/m$  phase of  $\text{Na}_3\text{MI}_6$  showed lower activation energy and higher ionic conductivity compared with the  $\bar{P}31c$  and  $R\bar{3}$  phases of  $\text{Na}_3\text{MBr}_6$ .  $\text{Na}_3\text{GdI}_6$  and  $\text{Na}_3\text{YI}_6$  exhibited activation energies of 0.30 and 0.34 eV and ionic conductivities of  $5.9 \times 10^{-4}$  and  $2.4 \times 10^{-4} \text{ S cm}^{-1}$  at room temperature, respectively. The activation energies, ionic conductivities and error bounds are listed in Tables 1 and S9.† The activation energy and Na ionic conductivity of the  $C2/m$  phase of  $\text{Na}_3\text{YI}_6$  showed good agreement with previous theoretical work<sup>39</sup> reporting 0.32 eV and  $3.5 \times 10^{-4} \text{ S cm}^{-1}$ , respectively. In the earlier study, the high ionic conductivity of  $C2/m$  phase was predicted for  $\text{Na}_3\text{YCl}_6$  and  $\text{Na}_3\text{YBr}_6$ ,<sup>38</sup> but  $P2_1/n$  phase was favorable structure for  $\text{Na}_3\text{YCl}_6$ , exhibiting low ionic conductivity approximately  $10^{-9} \text{ S cm}^{-1}$ .<sup>35</sup>

The isosurfaces of the Na-ion probability densities were plotted using an isosurface value of  $2P_0$  for  $\text{Na}_3\text{InBr}_6$  ( $\bar{P}31c$ ),  $\text{Na}_3\text{GdBr}_6$  ( $R\bar{3}$ ) and  $\text{Na}_3\text{GdI}_6$  ( $C2/m$ ) in Fig. 3(c–e), respectively, based on the Na-ion trajectories during 50 ps AIMD simulations at 800 K. As predicted from the relatively low values of  $E_a$  for the 1D paths in the  $\bar{P}31c$  and  $R\bar{3}$  phases (Fig. 2), Na-ion isosurfaces were more connected for 1D paths along the  $z$ -axis, as shown in Fig. 3(c and d), S12 and S13.† The higher  $E_a$  for the 3D paths in  $R\bar{3}$  phases inhibited long-range diffusion along the  $xy$  plane,



**Fig. 3** Arrhenius plots of Na-ion (a) diffusivity and (b) conductivity for  $\text{Na}_3\text{InBr}_6$ ,  $\text{Na}_3\text{GdBr}_6$ ,  $\text{Na}_3\text{YI}_6$  and  $\text{Na}_3\text{GdI}_6$ . The open symbols in (a) and (b) correspond to the ionic conductivities obtained by extrapolating from low- and high-temperature data, respectively. (c–e) Isosurfaces of the Na-ion probability densities (light blue) from 50 ps AIMD calculations at 800 K, plotted using an isosurface value of  $2P_0$  for (c)  $\text{Na}_3\text{InBr}_6$ , (d)  $\text{Na}_3\text{GdBr}_6$  and (e)  $\text{Na}_3\text{GdI}_6$ , where  $P_0$  is mean ionic probability density. The octahedra in (c–e) correspond to  $\text{InBr}_6$ ,  $\text{GdBr}_6$  and  $\text{GdI}_6$ , respectively.

**Table 1** Na ionic conductivities and activation energies of superionic Na halide SEs

Composition	Structure	$\sigma$ at 300 K ( $\text{mS cm}^{-1}$ )	$E_a$ (eV)
$\text{Na}_3\text{InBr}_6$	$P\bar{3}1c$	0.058	0.37
$\text{Na}_3\text{ErBr}_6$	$P2_1/n$	$10^{-6}$	N/A
$\text{Na}_3\text{GdBr}_6$	$R\bar{3}$	0.0012	0.50
$\text{Na}_3\text{YI}_6$	$C2/m$	0.24	0.34
$\text{Na}_3\text{YI}_6$ (ref. 39)	$C2/m$	0.35	0.32
$\text{Na}_3\text{GdI}_6$	$C2/m$	0.59	0.30
$\text{Na}_3\text{YBr}_3\text{I}_3$	$C2/m$	3.3	0.25
$\text{Na}_3\text{GdBr}_3\text{I}_3$	$C2/m$	7.5	0.21

resulting in the low ionic conductivity of  $R\bar{3}$ . The Na-ion diffusivity increased in the  $P\bar{3}1c$  phase for  $\text{Na}_3\text{MBr}_6$  as diffusion along the 3D paths is facilitated in this phase, as shown in Fig. S12.† In Fig. 3(e) and S14,† it can be seen that the isosurfaces in  $\text{Na}_3\text{GdI}_6$  are well connected through the 3D paths, verifying the high diffusivity in the  $C2/m$  phase.

Anion mixing was performed to increase the ionic conductivity of the  $C2/m$  phase  $\text{Na}_3\text{MI}_6$ , based on previous studies showing that Cl–Br mixing enhanced the ionic conductivity of  $\text{Li}_3\text{MCl}_6$  owing to the increase in disorder in chemical bonding.<sup>57,61,62</sup>  $\text{Na}_3\text{MBr}_x\text{I}_{6-x}$  ( $\text{M} = \text{Y}$  and  $\text{Gd}$ ) structures with the lowest energy among 100 randomly generated simulation cells were used for the calculations. The phase stability of  $\text{Na}_3\text{MBr}_x\text{I}_{6-x}$  was examined using the decomposition energy,  $E_d$ , as shown in Table S10.†  $\text{Na}_3\text{MBr}_x\text{I}_{6-x}$  was found to be a metastable phase and it showed a phase transition from  $C2/m$  to  $R\bar{3}$  as the ratio of Br in  $\text{Na}_3\text{MBr}_x\text{I}_{6-x}$  increased ( $x > 3$ ).

The Na-ion diffusivity and conductivity of the  $C2/m$  phase in  $\text{Na}_3\text{MBr}_3\text{I}_3$  ( $\text{M} = \text{Y}$  and  $\text{Gd}$ ) were evaluated using AIMD simulations, as shown in Fig. 4. The Arrhenius plot of the Na-ion diffusivity in Fig. 4(a) was obtained using the Na-ion MSD (Fig. S15†).  $\text{Na}_3\text{YBr}_3\text{I}_3$  and  $\text{Na}_3\text{GdBr}_3\text{I}_3$  exhibited activation energies of 0.25 and 0.21 eV and ionic conductivities of  $3.3 \times 10^{-3}$  and  $7.5 \times 10^{-3} \text{ S cm}^{-1}$  at room temperature, respectively. Anion mixing with Br in the  $C2/m$  phase of  $\text{Na}_3\text{MI}_6$  was found to be a valuable strategy to enhance the ionic conductivity. The predicted ionic conductivity of  $\text{Na}_3\text{GdBr}_3\text{I}_3$  ( $7.5 \text{ mS cm}^{-1}$ ) is the highest value among the studied Na halide SEs. The activation energies, ionic conductivities and error bounds for  $\text{Na}_3\text{YBr}_3\text{I}_3$  and  $\text{Na}_3\text{GdBr}_3\text{I}_3$  are listed in Tables 1 and S11.† The isosurfaces of the ionic probability densities for  $\text{Na}_3\text{GdI}_6$  and  $\text{Na}_3\text{GdBr}_3\text{I}_3$  are presented in Fig. 4(c) using an isosurface value of  $2P_0$  based on the Na-ion trajectories from 50 ps AIMD simulations at 800 K. The ionic probability densities for Na, Br and I are shown in light blue, orange and blue, respectively. The isosurfaces of the Na-ion probability densities for  $\text{Na}_3\text{GdBr}_3\text{I}_3$  were found to be more connected through the 3D paths than those for  $\text{Na}_3\text{GdI}_6$ , confirming the higher Na-ion diffusivity in  $\text{Na}_3\text{GdBr}_3\text{I}_3$ . Anion mixing likely increases disorder in the chemical bonding and enlarges the vibration of Br and I anions in the crystal lattice, which facilitates Na-ion migration. The isosurfaces of the ionic probability densities with views along various directions are shown in Fig. S16 and S17.†

The electrochemical stability window of  $\text{Na}_3\text{MX}_6$  ( $\text{X} = \text{Cl}$ , Br and I) was evaluated using a grand potential diagram as a function of the chemical potential of Na. As shown in Fig. 5,  $\text{Na}_3\text{MCl}_6$  and  $\text{Na}_3\text{MBr}_6$  display high oxidation potential of approximately 3.9 and 3.7 V, respectively, suggesting good



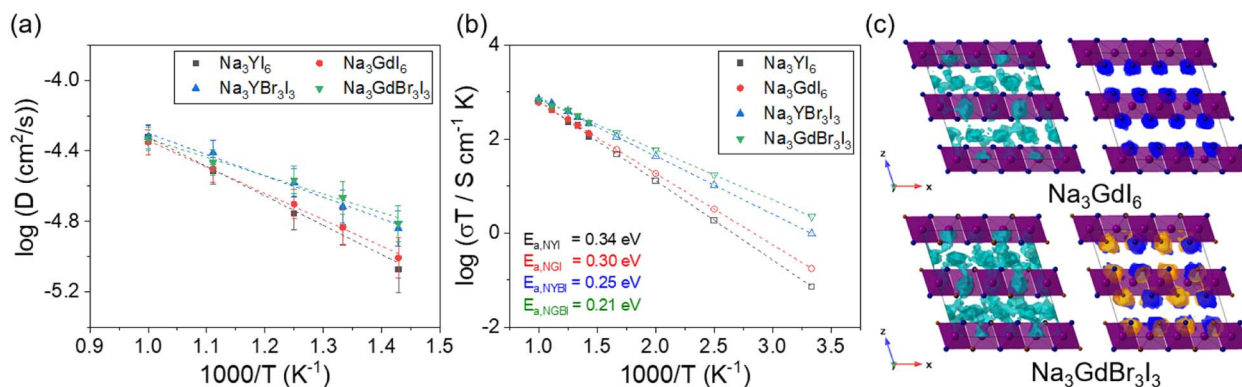


Fig. 4 Arrhenius plots of Na-ion (a) diffusivity and (b) conductivity for  $\text{Na}_3\text{YI}_6$ ,  $\text{Na}_3\text{GdI}_6$ ,  $\text{Na}_3\text{YBr}_3\text{I}_3$  and  $\text{Na}_3\text{GdBr}_3\text{I}_3$ . The open symbols in (b) correspond to the ionic conductivities obtained by extrapolating from high-temperature data. (c) Isosurfaces of the ionic probability densities for Na, Br and I (light blue, orange and blue, respectively) from 50 ps AIMD calculations at 800 K, plotted using an isosurface value of  $2P_0$  for  $\text{Na}_3\text{GdI}_6$  and  $\text{Na}_3\text{GdBr}_3\text{I}_3$ . The octahedra in (c) correspond to  $\text{GdBr}_x\text{I}_{6-x}$ .

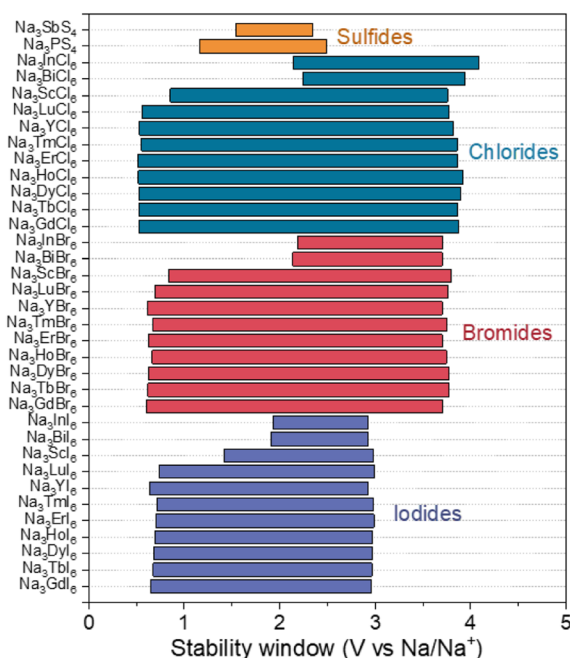


Fig. 5 Electrochemical stability windows of Na halide ( $\text{Na}_3\text{MX}_6$ ,  $X = \text{Cl}$ ,  $\text{Br}$  and  $\text{I}$ ) and sulfide ( $\text{Na}_3\text{PS}_4$  and  $\text{Na}_3\text{SbS}_4$ ) SEs.

electrochemical stability against oxidation at high voltages. We point out that, under real conditions, oxidation reactions typically occur at potentials higher than these theoretical limits owing to the kinetic barrier for the phase decomposition reaction and the presence of protective decomposition layers at the interface. Therefore,  $\text{Na}_3\text{MCl}_6$  and  $\text{Na}_3\text{MBr}_6$  could be applied to ASSBs with high-voltage cathodes and they show substantial advantages compared with sulfide SEs with low oxidation potentials ( $<2.5$  V), such as  $\text{Na}_3\text{PS}_4$  and  $\text{Na}_3\text{SbS}_4$ .<sup>63</sup>  $\text{Na}_3\text{MI}_6$  exhibits an oxidation potential of approximately 3.0 V, suggesting lower electrochemical stability against oxidation than  $\text{Na}_3\text{MCl}_6$  and  $\text{Na}_3\text{MBr}_6$ . Again, kinetic reaction barriers and decomposition layers may help to prevent the oxidation

reaction. Interface coatings could be applied to passivate the oxidative decomposition of  $\text{Na}_3\text{MI}_6$ .<sup>33</sup>

The reduction potentials of  $\text{Na}_3\text{MX}_6$  ( $X = \text{Cl}$ ,  $\text{Br}$  and  $\text{I}$ ) were found to depend on the identity of the M element, agreeing with previous studies on Li halides  $\text{Li}_3\text{MX}_6$  that electronegativity difference between M and X affected electrochemical stabilities.<sup>57</sup> Stronger electron localization between M and X would decrease the reduction potential. The reduction potentials of  $\text{Na}_3\text{MX}_6$  with p-block elements are approximately 2.1 V, whereas  $\text{Na}_3\text{MX}_6$  with group 3 elements and lanthanides exhibit a much lower reduction potential of approximately 0.6 V. Overall, however, the  $\text{Na}_3\text{MX}_6$  compounds generally show a wide electrochemical window. Reductive decomposition resulted in the formation of metallic compounds, as shown in Table S12,<sup>†</sup> enabling continuous reduction reactions of  $\text{Na}_3\text{MX}_6$  by conducting electrons.<sup>64</sup> Therefore, we suggest that interfacial coatings between the Na metal anode and  $\text{Na}_3\text{MX}_6$  would be required to inhibit the continuous reductive decomposition of  $\text{Na}_3\text{MX}$ . The oxidation and reduction potentials of  $\text{Na}_3\text{MX}_6$  and the phase equilibria at these potentials are summarized in Table S12.<sup>†</sup>

## Conclusions

In this study, we have provided design principles of superionic Na halide SEs through systematic analyses of the structural preference, phase stability, electrochemical stability and transport properties of  $\text{Na}_3\text{MX}_6$  ( $X = \text{Cl}$ ,  $\text{Br}$  and  $\text{I}$ ). The structures of  $\text{Na}_3\text{MX}_6$  are strongly dependent on the types and sizes of cations M and anions X, and the octahedral factors were found to be effective descriptors for predicting the stable phases of  $\text{Na}_3\text{MX}_6$ .  $\text{Na}_3\text{MX}_6$  generally exhibits  $P\bar{3}1c$ ,  $P2_1/n$ ,  $R\bar{3}$  and  $C2/m$  phases, while  $\text{Na}_3\text{MX}_6$  with relatively small M cations exhibits the  $\text{NaMX}_4$  ( $P2_12_12_1$ ) phase.  $\text{Na}_3\text{MCl}_6$  and  $\text{Na}_3\text{MBr}_6$  prefer the  $P\bar{3}1c$ ,  $P2_1/n$  and  $R\bar{3}$  phases and phase transitions from  $P\bar{3}1c$ – $P2_1/n$ – $R\bar{3}$  were found to occur with increasing size of M.  $\text{Na}_3\text{MI}_6$  showed octahedral factor values similar to those of the  $C2/m$  phase of  $\text{Li}_3\text{MCl}_6$ , indicating a preference for the  $C2/m$  phase

over the  $P\bar{3}1c$ ,  $P2_1/n$  and  $R\bar{3}$  phases. The effects of the structures of  $\text{Na}_3\text{MX}_6$  on Na-ion migration were investigated using the BVSE method and AIMD simulations. The energy barriers of Na-ion migration in the  $R\bar{3}$  and  $P2_1/n$  phases were found to be higher than those in the  $P\bar{3}1c$  phase for  $\text{Na}_3\text{MCl}_6$  and  $\text{Na}_3\text{MBr}_6$ , whereas the  $C2/m$  phase  $\text{Na}_3\text{MI}_6$  showed a lower barrier than the other phases. AIMD simulations likewise revealed that the  $P\bar{3}1c$  phase exhibits high ionic conductivity ( $\sim 10^{-5} \text{ S cm}^{-1}$ ) relative to the other phases of  $\text{Na}_3\text{MBr}_6$  and that the  $C2/m$  phase of  $\text{Na}_3\text{MI}_6$  shows even higher ionic conductivity ( $\sim 10^{-4} \text{ S cm}^{-1}$ ). Anion mixing with Br in  $\text{Na}_3\text{MI}_6$  further enhanced Na-ion migration, resulting in a superb ionic conductivity of  $7.5 \times 10^{-3} \text{ S cm}^{-1}$  for  $\text{Na}_3\text{GdBr}_3\text{I}_3$ , which is the highest value among the reported Na halide SEs.  $\text{Na}_3\text{MCl}_6$  and  $\text{Na}_3\text{MBr}_6$  exhibit natively high oxidation potentials, enabling compatibility with high-voltage cathodes ( $\sim 4 \text{ V}$ ), whereas interfacial coatings would be required to use  $\text{Na}_3\text{MI}_6$  with high-voltage cathodes. The material design principles in this work provide fundamental guidelines for the development of superionic Na halide SEs for high-voltage Na ASSBs.

## Conflicts of interest

There are no conflicts to declare.

## Acknowledgements

This work was supported by the institutional program of the Korea Institute of Science and Technology (Project No. 2E31861 and 2E31864) and the National Supercomputing Center with supercomputing resources including technical support (KSC-2022-CRE-0039). The work by K. K. and B. W. was performed under the auspices of the U.S. Department of Energy by Lawrence Livermore National Laboratory under Contract Number DE-AC52-07NA27344. B. W. acknowledges additional support from the Vehicle Technologies Office, Office of Energy Efficiency and Renewable Energy, U.S. Department of Energy.

## References

- 1 D. Larcher and J. M. Tarascon, *Nat. Chem.*, 2015, **7**, 19–29.
- 2 A. Manthiram, X. Yu and S. Wang, *Nat. Rev. Mater.*, 2017, **2**, 16103.
- 3 S. Randau, D. A. Weber, O. Kötzer, R. Koerver, P. Braun, A. Weber, E. Ivers-Tiffée, T. Adermann, J. Kulisch, W. G. Zeier, F. H. Richter and J. Janek, *Nat. Energy*, 2020, **5**, 259–270.
- 4 J. B. Goodenough and Y. Kim, *Chem. Mater.*, 2010, **22**, 587–603.
- 5 P. Albertus, S. Babinec, S. Litzelman and A. Newman, *Nat. Energy*, 2018, **3**, 16–21.
- 6 M. Cheng, Y. Wang, D. Zhang, S. Zhang, Y. Yang, X. Lv, J. Wang and Y. Nuli, *J. Energy Chem.*, 2023, **76**, 1–10.
- 7 S. Trano, F. Corsini, G. Pascuzzi, E. Giove, L. Fagiolar, J. Amici, C. Francia, S. Turri, S. Bodoardo, G. Griffini and F. Bella, *ChemSusChem*, 2022, **15**, e202200294.
- 8 F. Bella, S. De Luca, L. Fagiolar, D. Versaci, J. Amici, C. Francia and S. Bodoardo, *Nanomaterials*, 2021, **11**, 810.
- 9 M. Song, Y. Wang, B. Yu, W. Yang, G. Cheng, W. Cui and Z. Zhang, *Chem. Eng. J.*, 2022, **450**, 138176.
- 10 E. Manarin, F. Corsini, S. Trano, L. Fagiolar, J. Amici, C. Francia, S. Bodoardo, S. Turri, F. Bella and G. Griffini, *ACS Appl. Polym. Mater.*, 2022, **4**, 3855–3865.
- 11 A. Massaro, A. B. Muñoz-García, P. Maddalena, F. Bella, G. Meligrana, C. Gerbaldi and M. Pavone, *Nanoscale Adv.*, 2020, **2**, 2745–2751.
- 12 W. Hou, X. Guo, X. Shen, K. Amine, H. Yu and J. Lu, *Nano Energy*, 2018, **52**, 279–291.
- 13 Y. Lu, L. Li, Q. Zhang, Z. Niu and J. Chen, *Joule*, 2018, **2**, 1747–1770.
- 14 C. Zhao, L. Liu, X. Qi, Y. Lu, F. Wu, J. Zhao, Y. Yu, Y.-S. Hu and L. Chen, *Adv. Energy Mater.*, 2018, **8**, 1703012.
- 15 Y. Wang, S. Song, C. Xu, N. Hu, J. Molenda and L. Lu, *Nano Mater. Sci.*, 2019, **1**, 91–100.
- 16 T. Krauskopf, C. Pompe, M. A. Kraft and W. G. Zeier, *Chem. Mater.*, 2017, **29**, 8859–8869.
- 17 A. Banerjee, K. H. Park, J. W. Heo, Y. J. Nam, C. K. Moon, S. M. Oh, S.-T. Hong and Y. S. Jung, *Angew. Chem., Int. Ed.*, 2016, **55**, 9634–9638.
- 18 A. Hayashi, N. Masuzawa, S. Yubuchi, F. Tsuji, C. Hotehama, A. Sakuda and M. Tatsumisago, *Nat. Commun.*, 2019, **10**, 5266.
- 19 Z. Zhang, E. Ramos, F. Lalère, A. Assoud, K. Kaup, P. Hartman and L. F. Nazar, *Energy Environ. Sci.*, 2018, **11**, 87–93.
- 20 T. Fuchs, S. P. Culver, P. Till and W. G. Zeier, *ACS Energy Lett.*, 2020, **5**, 146–151.
- 21 Y. Xiao, Y. Wang, S.-H. Bo, J. C. Kim, L. J. Miara and G. Ceder, *Nat. Rev. Mater.*, 2020, **5**, 105–126.
- 22 Y. Lee, J. Jeong, H. J. Lee, M. Kim, D. Han, H. Kim, J. M. Yuk, K.-W. Nam, K. Y. Chung, H.-G. Jung and S. Yu, *ACS Energy Lett.*, 2022, **7**, 171–179.
- 23 N. Anantharamulu, K. Koteswara Rao, G. Rambabu, B. Vijaya Kumar, V. Radha and M. Vithal, *J. Mater. Sci.*, 2011, **46**, 2821–2837.
- 24 M.-C. Bay, M. Wang, R. Grissa, M. V. F. Heinz, J. Sakamoto and C. Battaglia, *Adv. Energy Mater.*, 2020, **10**, 1902899.
- 25 J. Liang, X. Li, K. R. Adair and X. Sun, *Acc. Chem. Res.*, 2021, **54**, 1023–1033.
- 26 X. Li, J. Liang, X. Yang, K. R. Adair, C. Wang, F. Zhao and X. Sun, *Energy Environ. Sci.*, 2020, **13**, 1429–1461.
- 27 S. Wang, Q. Bai, A. M. Nolan, Y. Liu, S. Gong, Q. Sun and Y. Mo, *Angew. Chem., Int. Ed.*, 2019, **58**, 8039–8043.
- 28 H. Kwak, S. Wang, J. Park, Y. Liu, K. T. Kim, Y. Choi, Y. Mo and Y. S. Jung, *ACS Energy Lett.*, 2022, **7**, 1776–1805.
- 29 T. Asano, A. Sakai, S. Ouchi, M. Sakaida, A. Miyazaki and S. Hasegawa, *Adv. Mater.*, 2018, **30**, 1803075.
- 30 X. Li, J. Liang, J. Luo, M. Norouzi Banis, C. Wang, W. Li, S. Deng, C. Yu, F. Zhao, Y. Hu, T.-K. Sham, L. Zhang, S. Zhao, S. Lu, H. Huang, R. Li, K. R. Adair and X. Sun, *Energy Environ. Sci.*, 2019, **12**, 2665–2671.



- 31 J. Liang, X. Li, S. Wang, K. R. Adair, W. Li, Y. Zhao, C. Wang, Y. Hu, L. Zhang, S. Zhao, S. Lu, H. Huang, R. Li, Y. Mo and X. Sun, *J. Am. Chem. Soc.*, 2020, **142**, 7012–7022.
- 32 L. Zhou, T.-T. Zuo, C. Y. Kwok, S. Y. Kim, A. Assoud, Q. Zhang, J. Janek and L. F. Nazar, *Nat. Energy*, 2022, **7**, 83–93.
- 33 S. Yu, H. Park and D. J. Siegel, *ACS Appl. Mater. Interfaces*, 2019, **11**, 36607–36615.
- 34 R. Schlem, A. Banik, M. Eckardt, M. Zobel and W. G. Zeier, *ACS Appl. Energy Mater.*, 2020, **3**, 10164–10173.
- 35 E. A. Wu, S. Banerjee, H. Tang, P. M. Richardson, J.-M. Doux, J. Qi, Z. Zhu, A. Grenier, Y. Li, E. Zhao, G. Deysher, E. Sebti, H. Nguyen, R. Stephens, G. Verbist, K. W. Chapman, R. J. Clément, A. Banerjee, Y. S. Meng and S. P. Ong, *Nat. Commun.*, 2021, **12**, 1256.
- 36 H. Kwak, J. Lyoo, J. Park, Y. Han, R. Asakura, A. Remhof, C. Battaglia, H. Kim, S.-T. Hong and Y. S. Jung, *Energy Storage Mater.*, 2021, **37**, 47–54.
- 37 D. Park, K. Kim, G. H. Chun, B. C. Wood, J. H. Shim and S. Yu, *J. Mater. Chem. A*, 2021, **9**, 23037–23045.
- 38 Y. Qie, S. Wang, S. Fu, H. Xie, Q. Sun and P. Jena, *J. Phys. Chem. Lett.*, 2020, **11**, 3376–3383.
- 39 H. Huang, H.-H. Wu, C. Chi, Y. Yang, J. Zheng, B. Huang and S. Wang, *J. Mater. Chem. A*, 2021, **9**, 26256–26265.
- 40 A. Bohnsack and G. Meyer, *Z. Anorg. Allg. Chem.*, 1997, **623**, 837–843.
- 41 G. Mairesse, P. Barbier and J.-P. Wignacourt, *Acta Crystallogr., Sect. B: Struct. Crystallogr. Cryst. Chem.*, 1979, **35**, 1573–1580.
- 42 T. Staffel and G. Meyer, *Z. Anorg. Allg. Chem.*, 1989, **574**, 107–113.
- 43 G. Kresse and J. Furthmüller, *Phys. Rev. B: Condens. Matter Mater. Phys.*, 1996, **54**, 11169–11186.
- 44 G. Kresse and D. Joubert, *Phys. Rev. B: Condens. Matter Mater. Phys.*, 1999, **59**, 1758–1775.
- 45 P. E. Blöchl, *Phys. Rev. B: Condens. Matter Mater. Phys.*, 1994, **50**, 17953–17979.
- 46 J. P. Perdew, K. Burke and M. Ernzerhof, *Phys. Rev. Lett.*, 1996, **77**, 3865–3868.
- 47 J. Klimeš, D. R. Bowler and A. Michaelides, *J. Phys.: Condens. Matter*, 2009, **22**, 022201.
- 48 S. P. Ong, W. D. Richards, A. Jain, G. Hautier, M. Kocher, S. Cholia, D. Gunter, V. L. Chevrier, K. A. Persson and G. Ceder, *Comput. Mater. Sci.*, 2013, **68**, 314–319.
- 49 G. Friedrich, H. Fink and H. J. Seifert, *Z. Anorg. Allg. Chem.*, 1987, **548**, 141–150.
- 50 M. Beran and G. Meyer, *Crystals*, 2011, **1**, 99–103.
- 51 G. Meyer, *Z. Anorg. Allg. Chem.*, 1984, **517**, 191–197.
- 52 H. Chen, L. L. Wong and S. Adams, *Acta Crystallogr., Sect. B: Struct. Crystallogr. Cryst. Chem.*, 2019, **75**, 18–33.
- 53 X. He, Y. Zhu, A. Epstein and Y. Mo, *npj Comput. Mater.*, 2018, **4**, 18.
- 54 Y. Liu, S. Wang, A. M. Nolan, C. Ling and Y. Mo, *Adv. Energy Mater.*, 2020, **10**, 2002356.
- 55 A. Jain, S. P. Ong, G. Hautier, W. Chen, W. D. Richards, S. Dacek, S. Cholia, D. Gunter, D. Skinner, G. Ceder and K. A. Persson, *APL Mater.*, 2013, **1**, 011002.
- 56 Y. Yu, Z. Wang and G. Shao, *J. Mater. Chem. A*, 2021, **9**, 25585–25594.
- 57 K. Kim, D. Park, H.-G. Jung, K. Y. Chung, J. H. Shim, B. C. Wood and S. Yu, *Chem. Mater.*, 2021, **33**, 3669–3677.
- 58 R. Xiao, H. Li and L. Chen, *Sci. Rep.*, 2015, **5**, 14227.
- 59 D. Park, H. Park, Y. Lee, S.-O. Kim, H.-G. Jung, K. Y. Chung, J. H. Shim and S. Yu, *ACS Appl. Mater. Interfaces*, 2020, **12**, 34806–34814.
- 60 A. D. Sendek, E. D. Cubuk, E. R. Antoniuk, G. Cheon, Y. Cui and E. J. Reed, *Chem. Mater.*, 2019, **31**, 342–352.
- 61 Z. Liu, S. Ma, J. Liu, S. Xiong, Y. Ma and H. Chen, *ACS Energy Lett.*, 2021, **6**, 298–304.
- 62 A. Zevgolis, B. C. Wood, Z. Mehmedović, A. T. Hall, T. C. Alves and N. Adelstein, *APL Mater.*, 2018, **6**, 047903.
- 63 H. Tang, Z. Deng, Z. Lin, Z. Wang, I.-H. Chu, C. Chen, Z. Zhu, C. Zheng and S. P. Ong, *Chem. Mater.*, 2018, **30**, 163–173.
- 64 L. M. Riegger, R. Schlem, J. Sann, W. G. Zeier and J. Janek, *Angew. Chem., Int. Ed.*, 2021, **60**, 6718–6723.